Microphotonic components for a *mm*-wave receiver

D.A. Cohen, A.F.J. Levi [*]

Department of Electrical Engineering, University of Southern California, DRB 118, Los Angeles, California, CA 90089-1111, USA

Abstract

A new microphotonic *mm*-wave receiver architecture with direct electrical-to-optical conversion is presented. The receiver uses high-Q RF and microphotonic electro-optic resonator components which are operated in simultaneous resonance. Initial results demonstrating modulation of an optical carrier at RF in the *mm*-wave range are reported. © 2001 Elsevier Science Ltd. All rights reserved.

Keywords: mm-wave receiver; LiNbO$_3$ modulator; Resonant detection; Microphotonic; Microdisk; Microsphere; Resonator

1. Introduction

RF receivers operating at *mm*-wave frequencies are of interest for indoor wireless and microcell wireless systems. Previous work has focused on the development and integration of all-electronic components to address these system needs [1]. Fig. 1 shows the basic building blocks of a conventional *mm*-wave electronic wireless receiver architecture consisting of an analog RF front-end and a digital signal-processing (DSP) module. Typically, most power is consumed in the analog monolithic microwave integrated circuit (MMIC). A state-of-the-art 60 GHz transmit/receive electronic analog RF front-end module developed by NEC consumes 1.2 W of which 0.4 W is used for the receiver [1]. Key components used by the NEC group are 0.15 μm gate-length AlGaAs/InGaAs heterojunction FETs with $f_{max} > 220$ GHz for electronic circuitry and a Ba-(Mg,Ta)O$_3$ dielectric resonator for a fixed-frequency, low-phase-noise, local oscillator (LO) used in the receiver module. Receiver functions include pass-band filtering, low-noise electronic amplification, down-conversion using an intermediate frequency oscillator, and low-pass filtering. The analog RF front-end of the receiver has a reported digital FSK data bandwidth of greater than 10 Mb/s (6 MHz equivalent analog bandwidth), sensitivity of 10 μW, and a volume of 900 mm^3. This work represents the present state-of-the-art. Any improvement in performance which results in significantly reduced power consumption and size will probably require a completely new approach to system design.

2. A *mm*-wave microphotonic architecture

In this paper, we propose and present initial experimental results which use a novel, non-electronic, microphotonic architecture for these wireless applications. By exploiting the unique properties of a microphotonic modulator, efficient, low-power, all-optical detection in a small volume can be achieved. Fig. 2 is a schematic of the proposed architecture. An electromagnetic wave is received at a RF antenna integrated with the modulator. This *mm*-wave signal feeds the electrodes of the microphotonic resonator where the RF signal is directly converted via the electro-optic response of the modulator to a 200 THz optical carrier frequency supplied by a distributed feedback (DFB) laser. The resulting phase-modulated optical signal is converted to amplitude-modulation through the use of a standard Mach–Zehnder configuration. After all-optical-signal processing, which may include filtering to suppress the

---
[*] Corresponding author. Tel.: +1-213-740-7318; fax: +1-213-740-9280.

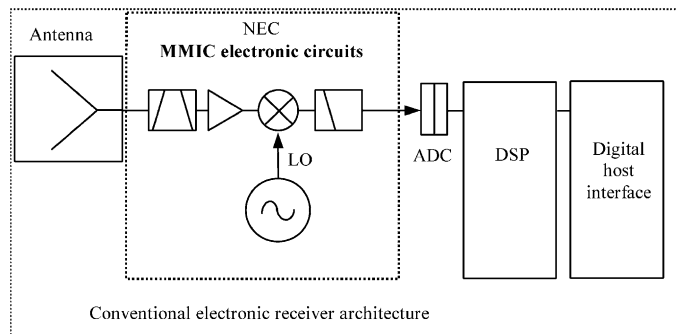*E-mail address:* alevi@usc.edu (A.F.J. Levi).

Fig. 1. Schematic of basic conventional wireless receiver architecture consisting of analog electronic circuitry in MMIC modules and a DSP module. An electromagnetic wave received at a RF antenna is pass-band filtered, amplified, and fed to a mixer. A LO also feeds the mixer whose output is filtered to obtain base-band.
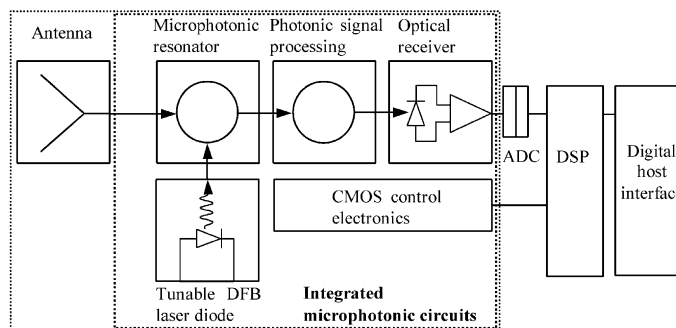

Fig. 2. Insertion of *mm*-wave microphotonic device technologies in future broad band heterodyne wireless architectures. An electromagnetic wave received at a RF antenna feeds electrodes of the microphotonic modulator. The modulator directly converts the RF signal to an optical carrier via the electro-optic effect. The resulting phase-modulated optical signal is converted to amplitude-modulation through the use of a standard Mach–Zehnder configuration. After conversion to the optical domain, the signal is processed using all-optical techniques before down-converting to base-band at the pin photodetector.

optical carrier, the intensity of the amplitude-modulated optical carrier is detected by the optical receiver which is sensitive only to base-band frequencies.

A microphotonic optical resonator is fabricated from an electro-optic material. The resonator's optical quality-factor, Q, is high to increase the effective interaction length of photons with an applied RF electric field. When combined with a simultaneously resonant RF electrical feed for voltage gain and a patterned electrode structure, high-sensitivity at *mm*-wave frequencies is achievable.

Fig. 3 illustrates the RF electric field spectrum as the signal progresses through the microphotonic architecture. The received RF electric field at the antenna is composed of a *mm*-wave carrier frequency, f_{RF}, with modulation side bands (shown in the figure using amplitude modulation (AM) as an example). The RF electric field modulates the optical field which is resonant within the electro-optic microphotonic resonator. As will be shown, if the RF carrier is a multiple of the

FSR of the optical cavity, the optical field in the cavity will be modulated efficiently at the RF carrier frequency. If the base-band modulation falls within the optical Q of the photonic resonator, the detected optical spectrum will consist of an optical carrier frequency, Ω_{opt}, optical sub-carrier frequencies $\Omega_{opt} \pm f_{RF}$, and optical base-band modulation about each sub-carrier frequency. The incident RF signal has thereby been converted from a RF carrier frequency to an optical carrier frequency. This modulated light may then be carrier suppressed by a passive optical filter and detected at the optical receiver. The low-pass frequency response of the optical receiver is used to detect and filter the base-band signal.

3. LiNbO₃ microphotonic resonator

There are many practical configurations for the microphotonic modulator. One particular approach uses a *z*-cut LiNbO₃ disk-shaped resonator with optically-
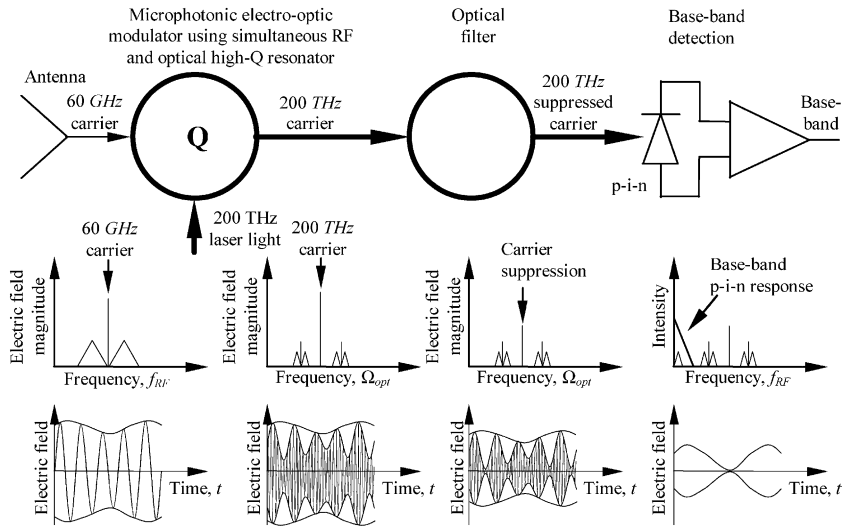
Fig. 3. A graphic showing the electric field spectrum as the signal progresses through the microphotonic architecture. A received *mm*-wave carrier frequency with AM side-bands modulates the optical field which is resonant within the electro-optic microphotonic resonator. The incident RF signal is converted from a RF carrier frequency to an optical carrier frequency. The detected optical spectrum consists of an optical carrier frequency, Ω_{opt}, optical sub-carrier frequencies $\Omega_{opt} \pm f_{RF}$, and optical base-band modulation about each sub-carrier frequency. This modulated light may then be carrier suppressed and detected at the optical receiver. The low-pass frequency response of the optical receiver is used to detect and filter the base-band signal.

polished curved side walls. The components are fabricated from the LiNbO$_3$ material system because of its high electro-optic coefficient, and its low loss at both optical and RF frequencies. LiNbO$_3$ is a negative uniaxial crystal with trigonal 3m crystal symmetry. The index of refraction along the extraordinary axis (*z*-axis) is $n_{opt} = 2.14$, at an optical wavelength $\lambda = 1.5$ µm, and greater than 5.1 µm at RF frequencies in the *mm*-wave regime [2,3].

Simultaneous resonance between optical and RF fields is possible inside the disk. Such resonance is achieved by confining a TE-polarized optical-field in a high-*Q* whispering-gallery mode (WGM) along the periphery of the disk, while metal electrodes feed RF power from a resonant electrical circuit. These metal electrodes are patterned above and below the equator of the disk to ensure good overlap of the resonant RF and optical fields. Optical input and output may be achieved by means of standard evanescent prism coupling with a power coupling coefficient κ [4]. Fig. 4 shows the schematic detail of this proposed receiver. An electromagnetic wave is received at a RF antenna integrated with the modulator. This *mm*-wave signal feeds the electrodes of the microphotonic resonator where the RF signal is directly converted via the electro-optic response of the modulator to a 200 THz optical carrier frequency supplied by a DFB laser. The resulting phase-modulated optical signal is converted to amplitude-modulation through use of a standard Mach–Zehnder configuration.

The intensity of the amplitude-modulated optical carrier is detected using an optical receiver whose response is sensitive only to base-band frequencies.

The microphotonic disk resonator can achieve optical *Q*s in excess of 4×10^6 resulting in an effective photon interaction length with the RF field of greater than 0.5 m for light of wavelength 1.5 µm. Although one sacrifices bandwidth with this resonant configuration, the effective photon interaction length, and hence voltage sensitivity, is more than 25 times that of a conventional Mach–Zehnder LiNbO$_3$ modulator.

3.1. Microphotonic optical resonator fabrication

Disk resonator geometry and polishing technique play an important role in determining optical *Q* and optical coupling. As shown in Fig. 5(a), the basic geometry of the LiNbO$_3$ resonator is a disk of radius *R*, where $1 \text{ mm} \leqslant R \leqslant 3 \text{ mm}$, and thickness *d*, where $0.2 \text{ mm} \leqslant d \leqslant 1 \text{ mm}$ for devices presently under test. The side wall of the disk is optically polished with a radius of curvature, *R'*, typically equal to the radius of the disk. The equator of the disk's curved side wall should be accurately maintained at height *d*/2.

While polishing optically flat surfaces with LiNbO$_3$ is a routine industrial procedure, polishing curved side walls to an optical finish in LiNbO$_3$ is not a standard practice. Fig. 5(b) is a photograph of a $R = 2$ mm,
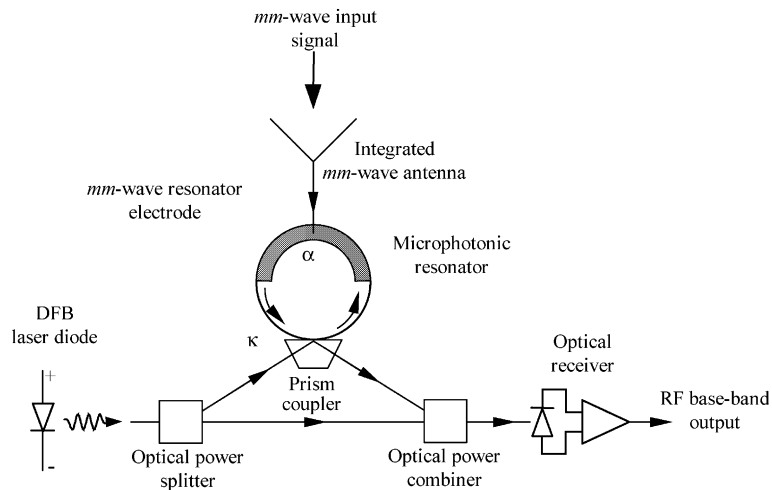
Fig. 4. Schematic detail of a microphotonic-based *mm*-wave RF detector. An electromagnetic wave received at a RF antenna feeds electrodes of the microphotonic modulator. The modulator directly converts the RF signal to an optical carrier via the electro-optic effect. The resulting phase-modulated optical signal is converted to amplitude-modulation through the use of a standard Mach–Zehnder configuration.

$d = 3.6$ mm disk which clearly shows the optically polished curved side walls of the disk. Fig 5(c) shows a smaller $R = 1$ mm, $d = 200$ μm thick z-cut LiNbO$_3$ disk prior to metalization. As will be discussed later, optical Q in excess of 4×10^6 near $\lambda = 1550$ nm wavelength is measured in high quality disks.

3.2. Optical coupling to the resonator

A significant challenge in the development of an optical resonator based system is zero-loss coupling of optical power both into and out of the resonator. This must be achieved to reduce coupling losses that are inherent in other systems such as conventional Mach–Zehnder LiNbO$_3$ modulators. Optical WGMs cannot be excited directly by simple propagating beams. Instead, coupling is achieved through indirect excitation of the WGMs using evanescent fields. There are numerous methods for evanescent coupling of light into guided modes, however prism coupling is particularly convenient because of the large refractive index of LiNbO$_3$. Basic prism-coupled optical configurations are shown schematically in Fig. 6.

The mechanism for coupling between prisms of index n_{prism} and disks with index n_{opt} is that of frustrated total internal reflection. The prominent component of the propagation constant $\beta_{n/m}$ for WGMs lies along the annulus of the disk for the high-Q modes we are interested in exciting [5,6]. To phase match with these modes, the angle of incidence of light with respect to the normal of the coupling face should be at an angle greater than or equal to $\theta = \arcsin(n_{opt}/n_{prism})$. This is fundamentally a result of Snell's law and results in the requirement that

$n_{prism} \geqslant n_{opt}$. This may be satisfied using diamond prisms of refractive index 2.4. Use of such prisms initially provided a total 25% optical coupling efficiency in the two-prism coupling scheme shown schematically in Fig. 6(b). Fig. 7(a) is a photograph of a prism coupler placed next to a LiNbO$_3$ disk viewed from above. The side view in Fig. 7(b) shows scattered laser light on only the right side of the disk periphery (the bright spots on the left side are prism reflections) which is consistent with a traveling wave excitation of the disk.

3.3. Optical spectrum of the microphotonic resonator

When TE-polarized WGMs are excited within the LiNbO$_3$ microphotonic resonator the detected optical spectrum shows peaks corresponding to the free spectral range (FSR) of the resonant cavity. This FSR is defined as $\Delta f_{FSR} \approx c/(n_{opt}2\pi R)$. It should be noted that $1/\Delta f_{FSR}$ is equal to the round trip time of the cavity $\tau_{disk} = (n2\pi R)/c$. Fig. 8(a) shows a typical experimental result using the two-prism coupling scheme and a tunable DFB laser to scan the entire FSR of the disk. A disk of diameter $2R = 5.85$ mm, and thickness $d = 0.7$ mm exhibited a FSR of 7.57 GHz (60.6 pm) for TE optical modes. Within the uncertainty of the measured disk radius, these values agree with the equation for Δf_{FSR}.

3.4. Optical losses, and the quality factor, Q

Optical losses and photon lifetime of the resonator can be extrapolated from the quality factor Q. The quality factor is defined as $Q \equiv \Omega\, E/P = f/\Delta f_{FWHM} = \lambda/\Delta\lambda_{FWHM} = \Omega\tau_c$, where $\Omega = 2\pi f$, E is the energy stored
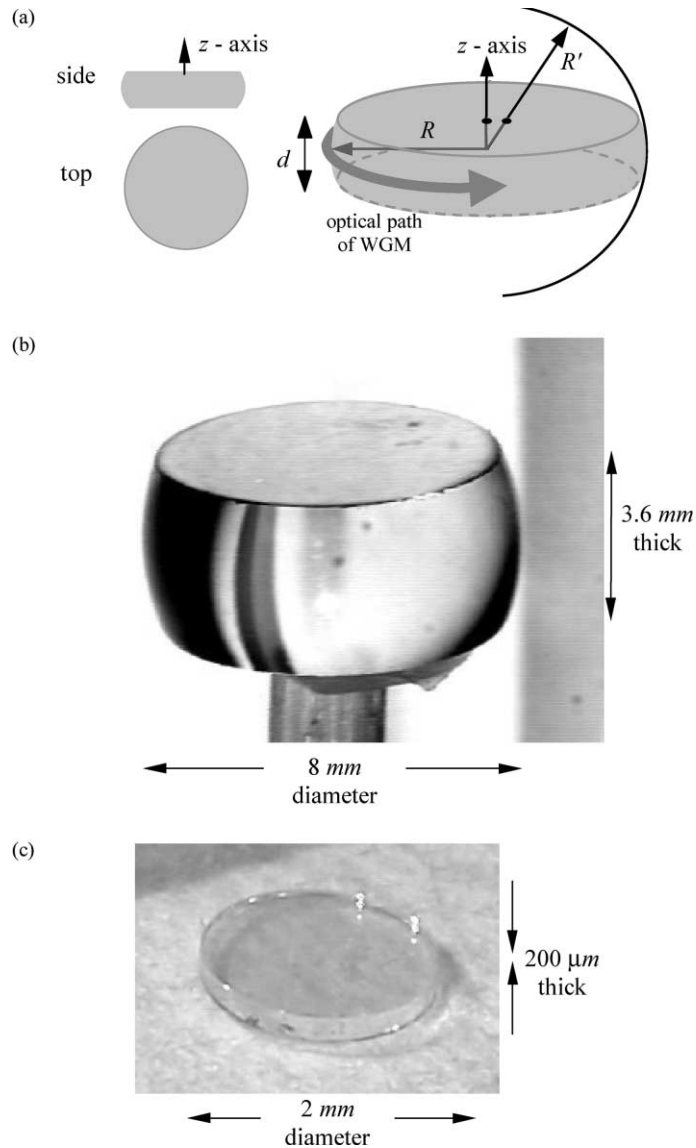
Fig. 5. (a) Sketch of the geometry of a microdisk indicating disk radius R, disk thickness d and curved side walls with radius of curvature R'. (b) Photograph of a small z-cut LiNbO$_3$ disk-shaped resonator. The size of the disk is indicated. (c) Photograph of a large z-cut LiNbO$_3$ disk-shaped resonator with solid-gold top and bottom flat electrodes and optically-polished curved side walls. The size of the disk is indicated.

in the resonant mode, P is the power dissipated in the cavity, Δf_{FWHM} is the full-width at half maximum of the spectral peak at optical frequency f, and τ_c is the $1/e$ photon lifetime. The measured optical Q of a LiNbO$_3$ disk with diameter 5.85 mm is shown in Fig. 8(b). This mode was measured using the two-prism coupling scheme and a wavelength tunable DFB laser input with linewidth < 0.5 MHz.

The total measured optical Q including the effects of coupler loading is greater than 4×10^6 near $\lambda = 1550$ nm

wavelength and $\lambda f_{\text{FWHM}} = 48$ MHz. We find for this Q, the photon cavity lifetime is $\tau_c = 3.4$ ns. The effective number of round trips per photon from $c\tau_c/n_{\text{opt}}2\pi R$ is approximately 26. Assuming the Q is dominated by optical scattering at the disk edge, we define a distributed loss constant α as the loss per unit length, where $\alpha = n_{\text{opt}}/(c\tau_c) = 0.02$ cm^{-1}. This is 10–100 times better than typical waveguide scattering in semiconductors, and demonstrates an ability to obtain a high-quality, low-loss optical polish.
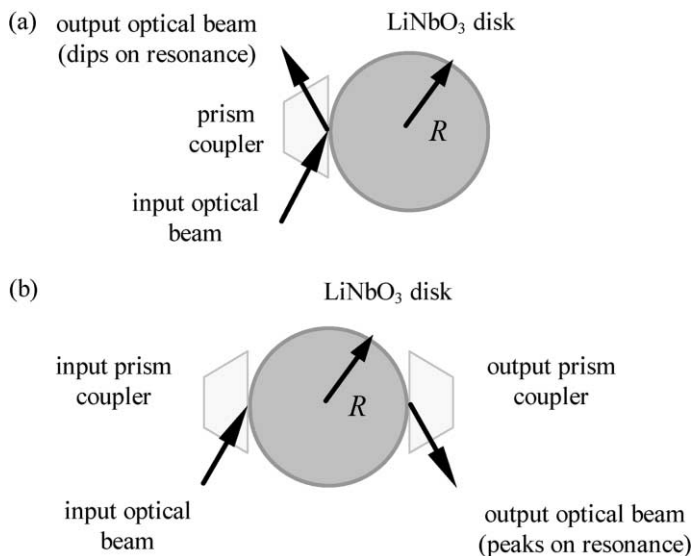
Fig. 6. Sketch showing (a) single prism coupling and (b) two prism coupling of the optical field to the microphotonic resonator.
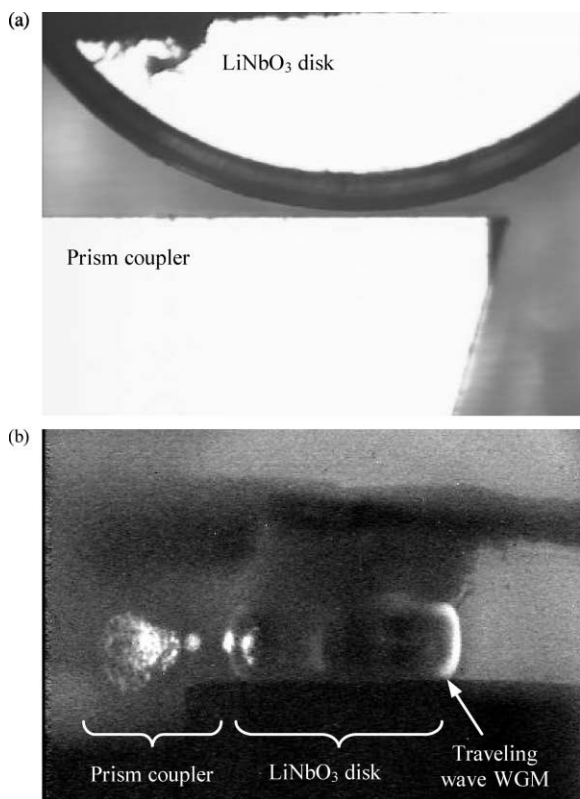

Fig. 7. (a) Photograph of LiNbO$_3$ disk and prism-coupler viewed from above. (b) Infrared side view of disk resonator and prism showing optical coupling at $\lambda = 1550$ nm wavelength. Coupled laser light on the disk periphery is indicated by the arrow.
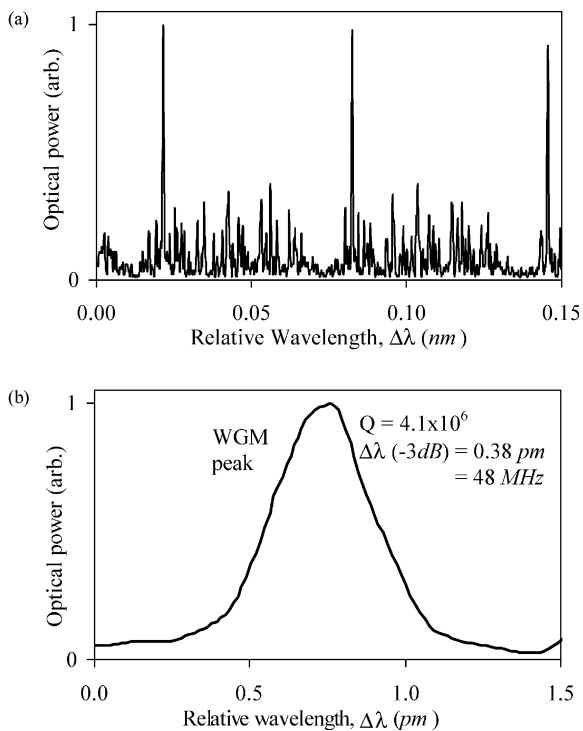

Fig. 8. (a) Measured optical spectrum of a z-cut LiNbO$_3$ disk-shaped resonator. The peaks in the spectrum correspond to WGM of the disk. (b) Measured optical resonance near wavelength $\lambda = 1550$ nm of a z-cut LiNbO$_3$ disk-shaped resonator with gold electrodes and optically polished curved side walls. The measured Q of this device is in excess of 4×10^6.

4. Static electro-optic response of the LiNbO₃ microphotonic modulator

4.1. Electrical coupling to the microphotonic resonator using metal electrodes

One method to couple the electric field detected at the RF antenna to the microphotonic modulator is to pattern metal electrodes onto the LiNbO₃ disk. These electrodes may be part of a resonant RF circuit used to amplify the RF electric field, thereby increasing optical modulation. Since the WGM nature of the optical field strongly confines light to the edge of the disk, the electrodes can be patterned to significantly overlap the optical and electromagnetic fields inside the disk. Optimizing the overlap improves RF field sensitivity. Fig. 9(a) is a photograph of a thin z-cut LiNbO₃ disk-shaped resonator with optically polished curved side walls and gold electrodes placed in an annulus around the disk to increase the overlap of RF and optical fields. In addition, the RF electric field on the metal electrodes of the disk interacts with photons via the electro-optic effect and not a resistive electrical load. Consequently no damping of the RF Q due to a load resistor occurs for the LiNbO₃ disk. This is an inherent property of the

optical isolation provided by use of a LiNbO₃ resonator in the system.

4.2. DC voltage response

Ideally, the electro-optic effect in z-cut LiNbO₃ changes only the optical refractive index of the medium as a function of time, $n(t)$. For time $t > 0$ the resonant frequency of light in the cavity changes adiabatically as the index of refraction changes, $f(t) \sim f_0 n_0 / n(t)$, where f_0 is the unperturbed resonant frequency at time $t \leqslant 0$ and n_0 is the refractive index at time $t \leqslant 0$. Application of a DC voltage V_{DC} along the crystal's z-axis will shift the WGM resonant wavelength $\lambda_0 = 2\pi c / \Omega_0$ due to a change of refractive index Δn_{opt}. If the applied DC electric field is $E_{DC} = V_{DC}/d$, where d is the thickness of the disk, the electro-optic effect changes the refractive index along the z-axis by $\Delta n_{opt} = n_e^3 \, r(33) E_{DC}/2$, where $r(33) \sim 30.8 \times 10^{-12}$ m/V s at an optical wavelength $\lambda = 1.55$ μm. Given that m_{opt} is approximately the number of optical wavelengths along the disk circumference, from $m_{opt}\lambda = n_{opt}2\pi R$, the shift of the WGM resonant wavelength by a DC electric field is $\Delta\lambda_{DC} = 2\pi R \Delta n_{opt}/m_{opt}$.

To demonstrate electrically controlled optical resonance tuning in a microphotonic disk, an electric field is applied perpendicular to the top disk face (parallel to the z-axis). This was accomplished by applying a DC voltage to a metal ring on a LiNbO₃ resonator similar to that shown in Fig. 9(a). As shown in Fig. 9(b), a TE-polarized mode may be tuned 70 MHz (0.56 pm) with an applied DC electric field of 10.8 V/mm.

5. RF electro-optic modulation using a microphotonic resonator

5.1. The patterned metal electrode structure

RF modulation frequency of the microphotonic resonator is determined by the FSR of the optical resonator and the spatial pattern of the metal electrode structure. The frequency of the RF carrier f_{RF} should be an integral multiple m of the optical FSR, f_{FSR}, where $f_{FSR} = 1/\tau_{disk} = c/n_{opt}2\pi R$, τ_{disk} is the optical round-trip time of the disk, and R is the disk radius [7]. A periodic metal electrode structure permits operation of the modulator well beyond a typically 20 GHz –3 dB roll-off of conventional commercial LiNbO₃ modulators. This is understood by first considering an ideal single optical-pass configuration ($\kappa = 1$). The modulation response of a solid-ring electrode is just that of a conventional Mach–Zehnder interferometer (Fig. 10(a)). We assume a radius $R = 3.18$ mm which gives a FSR of $f_{FSR} = 7.03$ GHz. As expected, the modulator has a sinc function response with little efficiency at large values of f_{RF}. The
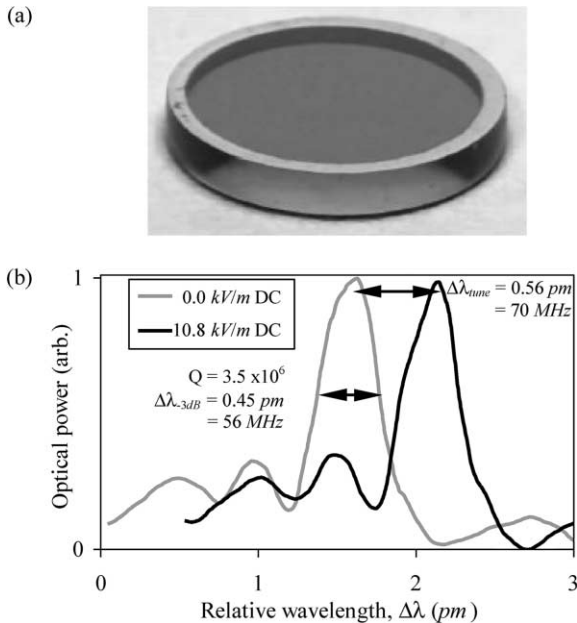

(a)

(b)

Fig. 9. (a) Photograph of a z-cut LiNbO₃ disk-shaped resonator with optically polished curved side walls. Gold electrodes are placed in an annulus around the disk to increase the overlap of electrical bias and optical fields. The dimensions of the disk are radius $R = 5.8$ mm and thickness $d = 0.74$ mm. (b) Measured shift in resonant wavelength due to application of 8 V DC bias between the top and bottom electrodes of the disk shown in (a). The change in resonant wavelength is 0.07 pm/V.
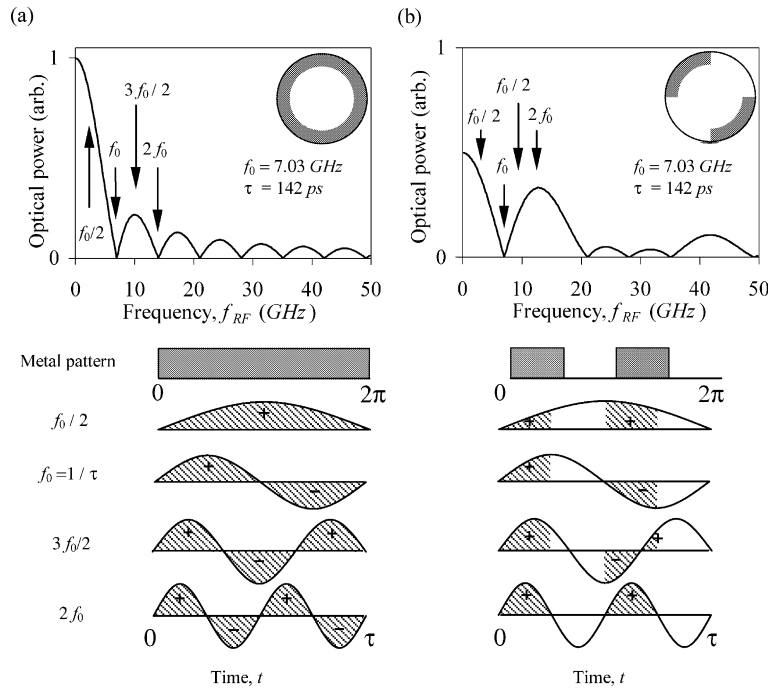
Fig. 10. Calculated response of a microphotonic-based opto-electronic modulator with the indicated periodic metal-electrode structures and $f_{FSR} = 7$ GHz. (a) A $R = 3.18$ mm LiNbO$_3$ disk modulator with $\kappa = 1$ and a continuous ring-electrode. (b) $\kappa = 1$ optical coupling with a split 4-segment ring-electrode showing a peak in opto-electronic response at 14 GHz.

first null in the frequency response is when the round-trip time of the optical wave τ_{disk} equals the period $T = 1/f_{RF}$. This occurs because during the positive part of the RF electric field's cycle, the disk's optical field obtains a positive phase-shift ("+" in Fig. 10(a)) which is exactly canceled during the negative cycle ("−" in Fig. 10(a)). Similarly, when the applied RF frequency is any integer multiple m of the optical round-trip frequency ($f_{RF} = m/\tau_{disk}$), a null in the frequency response results. Modulation may be enhanced at such a null if the electrode structure is modified as, for example, shown in Fig. 10(b). In this case, while the RF electric field at frequency $f_{RF} = 2f_{FSR}$ is positive, light passing through a region with an electrode receives a positive phase-shift. While the RF electric field is negative, the light passes through a region without an electrode and receives no phase-shift. Results of calculations given in Fig. 10(b) show that use of such a patterned two-electrode structure enables efficient modulation near 14 GHz. The loss in base-band efficiency in Fig. 10(b) compared to the ring electrode of Fig 10(a) is a result of only half the disk being patterned. In addition, the relative response at the resonant frequency compared to base-band is 0.63 indicating the potential for efficient modulation. A larger modulation response at base-band results because a photon will encounter a larger average electric field during a single round trip. This is because the time constant determining this response is the round trip time

$\tau_{disk} = 1/f_{FSR}$ of the disk. If the applied RF frequency, f_{RF} is much less than f_{FSR}, a photon will make many round trips within one frequency cycle time $1/f_{RF}$, and thereby encounters a relatively uniform RF field. At higher frequencies, a photon will encounter a varying RF field during a single round trip, reducing the average electric field seen.

For the optically resonant case ($\kappa < 1$), the modulated optical electric field resulting from multiple round-trips may be obtained from the expressions

$$E_{out}(t) = \left[\sqrt{(1 - \kappa)} E_{in}(t) \right.$$
$$\left. - \frac{\kappa}{\sqrt{(1 - \kappa)}} \sum_{n=1}^{\infty} r^n e^{-jF_n(t - n\tau_{disk})} E_{in}(t - n\tau_{disk}) \right]$$

$$F_n(t - n\tau_{disk}) = \left[\sum_{i=0}^{n-1} \phi(t - i\tau_{disk}) \right]$$

where $E_{out}(t)$ is the electric field exiting the prism, $E_{in}(t)$ is the field entering the prism, n is the round trip number, $r = \alpha^{1/2}(1 - \kappa)^{1/2}$, α is the optical single-pass power transmission, and $\phi(t)$ is the optical single-pass phase-shift resulting from the applied RF field. The above equation simplifies when the applied RF electric field

frequency is the same as the optical FSR of the disk ($f_{RF} = 1/\tau_{disk}$). In this case, the expression becomes

$$E_{out}(t) = \left[\sqrt{(1-\kappa)} - \frac{\kappa}{\sqrt{(1-\kappa)}} \frac{\rho e^{-j\phi(t)}}{1 - \rho e^{-j\phi(t)}} \right] E_i(t)$$

where $\rho = r\exp(\Omega_{opt}\tau_{disk})$, and Ω_{opt} is the optical frequency.

As shown in Fig. 11(a) for the resonant solid-ring electrode, high optical-Q results in a summation of multiple round-trips that further suppresses modulation
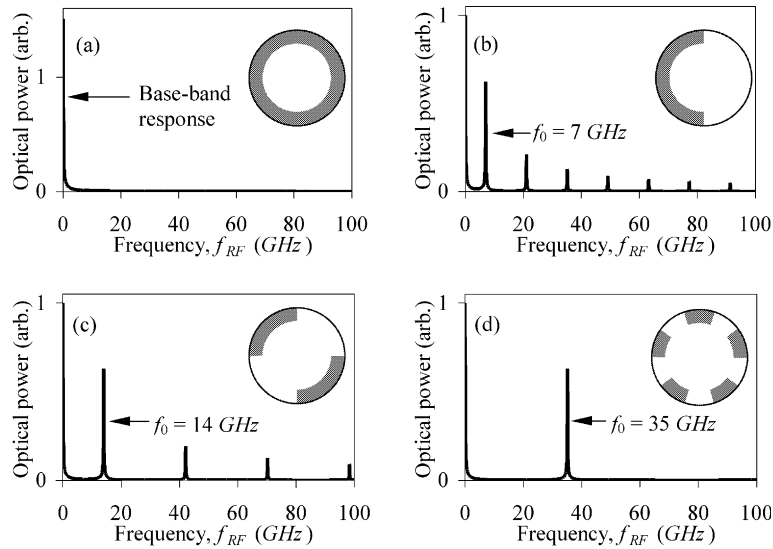

Fig. 11. Calculated response of a microphotonic-based opto-electronic modulator with the indicated periodic metal electrode structures. (a) A $R = 3.18$ mm LiNbO$_3$ disk modulator with $\kappa = 0.05$ and a continuous ring electrode. (b) $\kappa = 0.05$ with a split 2-segment ring-electrode showing resonant opto-electronic response at 7 GHz. (c) $\kappa = 0.05$ with 4 segments and response at 14 GHz. (d) $\kappa = 0.05$ with 10 segments showing response at 35 GHz.
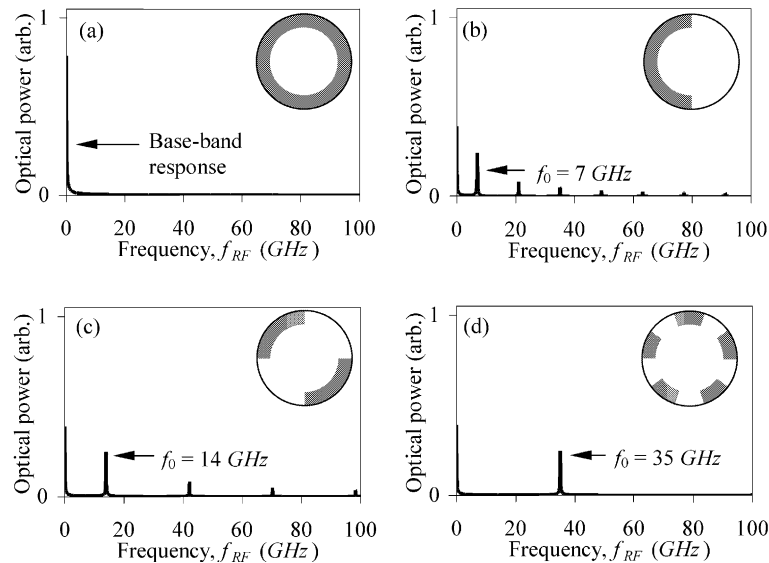

Fig. 12. Calculated response of a microphotonic-based opto-electronic modulator with the indicated periodic metal electrode structures and finite scattering coefficient $\alpha = 0.01$ cm^{-1}. (a) A $R = 3.18$ mm LiNbO$_3$ disk modulator with $\kappa = 0.05$ and a continuous ring electrode. (b) $\kappa = 0.05$ with a split 2-segment ring-electrode showing resonant opto-electronic response at 7 GHz. (c) $\kappa = 0.05$ with 4 segments and response at 14 GHz. (d) $\kappa = 0.05$ with 10 segments showing response at 35 GHz.
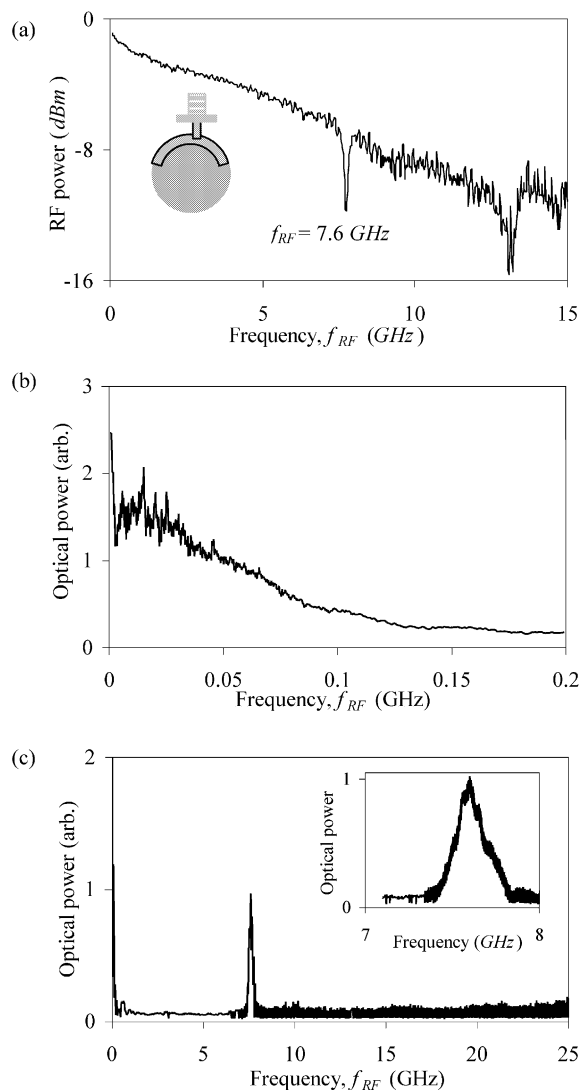
(a)

f_{RF} = 7.6 GHz

(b)

(c)

Fig. 13. Measured results showing optical modulation of a 5.8 mm diameter, 0.74 mm thick LiNbO$_3$ microphotonic modulator at 7 GHz. (a) The reflected swept RF excitation resonance of the resonant electrode structure show in the inset. (b) Detected optical response at base-band frequencies versus a swept RF input. (c) Detected optical response versus a swept RF input. The resulting modulation peak is at 7.6 GHz with a measured bandwidth of 150 MHz.
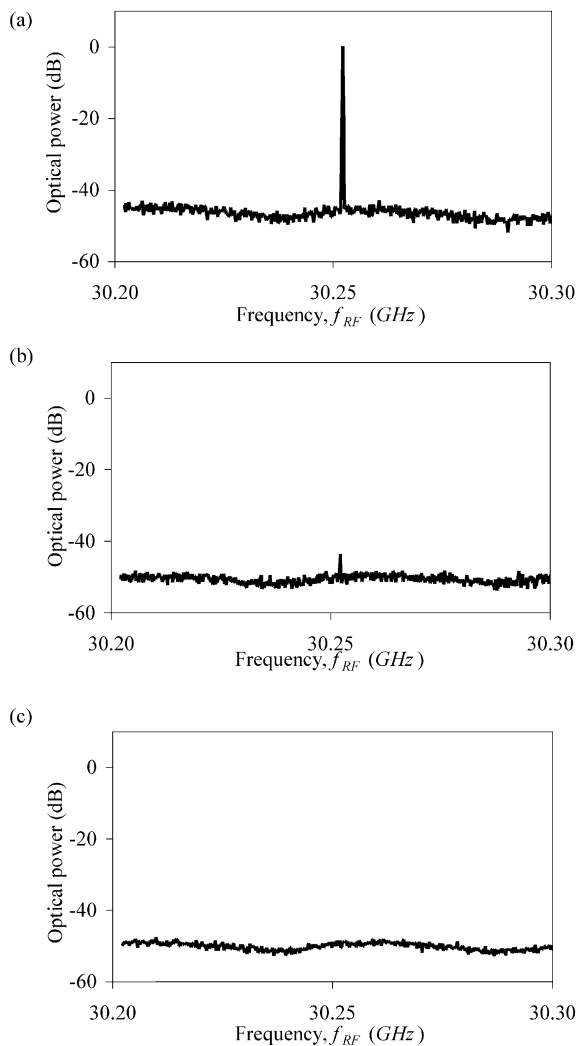
(a)

(b)

(c)

Fig. 14. (a) Measured results showing optical modulation of a 5.8 mm diameter, 0.74 mm thick LiNbO$_3$ microphotonic modulator at 30.25 GHz for a CW RF input. (b) Detected optical response when the optical wavelength is tuned off the optical resonance. (c) Detected optical response when the applied RF field is tuned off the RF resonant frequency.

efficiency at finite frequency. Fig. 11(b)–(d) illustrate how a change in the metal electrode pattern shifts the resonant response to higher frequencies with little decrease in efficiency. This demonstrates that disk size, in itself, does not limit *mm*-wave operation.

Fig. 12 shows the simulated response for a finite-round trip electric field loss α of the disk. A distributed value of α = 0.01 cm^{-1} is typical for the experimental results presented in this paper. The modulation effi-

ciency of the lossy resonant case at large RF frequency is found to be about 25% that of the zero-loss base-band modulation shown in Fig. 11. This is a combination of the 0.63 resonant frequency to base-band efficiency, and finite α loss. A factor of two improvement in modulation efficiency is achievable by pattering electrodes in a differential (push-pull) configuration. Unpatterned regions of the disks shown in Fig. 11 could be patterned and fed by a π phase-shifted RF field. This converts the negative phase-shift incurred during the negative cycle of the RF field to a positive phase shift, thereby doubling the optical modulation efficiency.

5.2. Experimental results of RF modulation

To confirm our simulations, we show experimental results in Fig. 13. Light of wavelength 1.55 μm is coupled into a $2R = 5.8$ mm diameter LiNbO$_3$ disk with a resulting FSR of 7.6 GHz. A microstrip electrode is placed on top of the LiNbO$_3$ disk and excited with a RF field using a SMA microstrip launcher. Using a network analyzer, we tune the fundamental resonant frequency of the microstrip electrode to match the FSR of 7.6 GHz by monitoring the dip in the reflected RF excitation response (Fig. 13(a)). Fig. 13(b) and (c) demonstrate the detected modulated optical power from the LiNbO$_3$ microphotonic modulator. We see that the 7.6 GHz optical modulation is 60% that of base-band modulation as expected by simulation discussed in Section 5.1. In addition, the RF bandwidth of 150 MHz matches closely with the measured optical Q of 1.3×10^6.

5.3. Experimental results of mm-wave modulation

As indicated through simulation, modulation can be achieved at an integral number times the optical FSR of the disk by changing the period of the metal electrodes. This is demonstrated through experiment where we achieve *mm*-modulation as shown in Fig. 14(a). By modifying the resonant periodicity of the metal electrodes on a LiNbO$_3$ microphotonic modulator, *mm*-wave modulation at a frequency of 30.25 GHz is obtained. This frequency is approximately four times the optical FSR of 7.6 GHz as expected. Fig. 14(a) shows both RF and optical electrical fields simultaneously tuned on resonance. To confirm that modulation is a result of simultaneous resonance of RF and optical electric fields within the disk, we individually detune the applied RF frequency, and optical wavelength from that of resonance. In Fig. 14(b) we keep the RF on resonance, while tuning the optical wavelength off resonance, showing that there is only residual modulation at less than −40 dB as compared with the simultaneously on resonance modulation. This is a result of optical excitation of low-Q higher-order modes while tuned off resonance. Fig. 14(c) shows complete loss of modulation as the RF electric field is detuned from resonance.

6. Conclusion

A new type of *mm*-wave RF receiver architecture with direct electrical-to-optical conversion has been described. Simulation of a microphotonic modulator which uses simultaneous resonance of optical and RF electric fields demonstrates that efficient modulation is achievable at *mm*-wave frequencies through the use of a periodic metal electrode. In addition, experimental results confirm our model and demonstrate modulation at *mm*-wave frequencies.

References

[1] Ohata K, Inoue T, Funabashi M, Inoue A, Takimoto Y, Kuwabara T, Shinozaki S, Maruhashi K, Hosaya K, Nagai H. IEEE Trans Microwave Theory Techn 1996;44:2354–60.
[2] Robertson WM, Arjavalingam G, Kopcsay GV. Electron Lett 1991;27:175–6.
[3] Properties of Lithium Niobate. EMIS Data Reviews Series No. 5. INSPEC, London. 1989 (ISBN 085296 482 X).
[4] Tien PK, Ulrich R. J Opt Soc Am 1970;60:1325–37.
[5] Hill SC, Benner RE. In: Barber PW, Chang RK, editors. Optical effects associated with small particles, Singapore: World Scientific; 1988. p. 3.
[6] Braginsky VB, Ilchenko VS. Phys Lett 1989;A-137:393–7.
[7] Kourogi M, Nakagawa K, Ohtsu M. IEEE J Quantum Electron 1993;29:2693–701.